

# JAAS

Accepted Manuscript



This is an *Accepted Manuscript*, which has been through the Royal Society of Chemistry peer review process and has been accepted for publication.

*Accepted Manuscripts* are published online shortly after acceptance, before technical editing, formatting and proof reading. Using this free service, authors can make their results available to the community, in citable form, before we publish the edited article. We will replace this *Accepted Manuscript* with the edited and formatted *Advance Article* as soon as it is available.

You can find more information about *Accepted Manuscripts* in the [Information for Authors](#).

Please note that technical editing may introduce minor changes to the text and/or graphics, which may alter content. The journal's standard [Terms & Conditions](#) and the [Ethical guidelines](#) still apply. In no event shall the Royal Society of Chemistry be held responsible for any errors or omissions in this *Accepted Manuscript* or any consequences arising from the use of any information it contains.

1  
2  
3 Cite this: DOI: 10.1039/c0xx00000x4  
5 www.rsc.org/xxxxxx

ARTICLE TYPE

6  
7 **Application of a Spoked Channel Array to confocal X-ray fluorescence**  
8 **imaging and X-ray absorption spectroscopy of medieval stained glass**9  
10  
11 **Sanjukta Choudhury,<sup>a</sup> Josef Hormes,<sup>b</sup> David N. Agyeman-Budu,<sup>c</sup> Arthur R. Woll,<sup>c</sup> Graham N. George,<sup>a</sup>**  
12 **Ian Coulthard,<sup>d</sup> and Ingrid J. Pickering<sup>a\*</sup>**13  
14 <sup>5</sup> *Received (in XXX, XXX) Xth XXXXXXXXX 20XX, Accepted Xth XXXXXXXXX 20XX*

15 DOI: 10.1039/b000000x

16  
17 Confocal X-ray fluorescence imaging can determine the spatial distribution of elements in a depth-  
18 selective manner. The closely related technique of confocal X-ray absorption spectroscopy can reveal the  
19 chemical form of an element at a specific volume element in three dimensional space. Confocal  
20 measurement offers increased accuracy and avoids physical sectioning or ablative depth profiling  
21 methods, thus preserving sample integrity. At present, a polycapillary mounted on the detector is the  
22 common optical element used to complete the confocal configuration. Here we demonstrate  
23 implementation of a novel collection optic, a lithographically fabricated Spoked Channel Array, to  
24 achieve the confocal configuration at beamline 20-ID, Advanced Photon Source. The advantages of  
25 employing Spoked Channel Arrays include improved spatial resolution and energy-independent probing  
26 volume. By employing this optic, three dimensional distributions of Fe, Ca and Mn and the localized  
27 chemical form of Fe were measured in the intact corrosion layer of an ancient stained glass sample  
28 obtained from 13<sup>th</sup> Century Paderborn Cathedral, Germany. Implementation of the optic enabled superior  
29 resolution depth selectivity in the intact corrosion layer and measurement of elemental distribution and  
30 speciation in a highly localized manner within the layer with improved signal to noise. The results show  
31 that both the composition and the chemical form vary as a function of three-dimensional location in the  
32 corrosion layer. This observation is contrary to expectations from simple corrosion models assuming  
33 leaching processes and indicates that metal chemistry in these layers is quite complex.  
3435  
36 **Introduction**37  
38 The implementation of synchrotron based techniques to  
39 investigate artefacts of historical interest is an area of significant  
40 growth. Bright and tunable synchrotron X-rays enable greatly  
41 improved sensitivity in trace elemental detection together with  
42 techniques not possible using conventional X-ray sources. X-ray  
43 fluorescence imaging (XFI) is a non-destructive tool for studying  
44 two-dimensional trace element distribution.<sup>1</sup> Confocal XFI,<sup>2,3</sup>  
45 a more recent variant, enables depth selective investigation of the  
46 spatial distribution of elements from a thick or intact sample with  
47 improved spatial resolution, and is particularly useful for fragile  
48 or valuable objects for which sectioning is challenging or  
49 undesirable. Although confocal micro-analysis is a relatively new  
50 technique, its application in investigating cultural heritage  
51 samples is of increasing interest due to the non-destructive nature  
52 and depth-profiling capability of this method. Some examples of  
53 such studies include: paint layers in ancient Indian Mughal  
54 miniatures,<sup>4</sup> depth profiling of historic paintings,<sup>3</sup> Chinese faux  
55 bamboo paint,<sup>5</sup> corrosion layers of reverse glass paintings,<sup>6</sup>  
56 Japanese lacquerware *Tamamushi-nuri*,<sup>7</sup> Portuguese polychrome  
57 glazed ceramics,<sup>8</sup> and Persian polychrome underglaze painted  
58 tiles.<sup>9</sup>39  
40 Confocal detection requires the use of an additional focusing  
41 optic placed in front of the detector in conjunction with the  
42 focusing optic at the incident side. The spatial resolution of a  
43 confocal XFI experiment is defined by the size of the probing  
44 volume, which depends on the focal spot sizes of the incident and  
45 collection focusing optics.<sup>3</sup> Although a number of optics are in  
46 use for focusing the incident synchrotron X-ray beam, a  
47 polycapillary has been the predominant choice of optic for the  
48 collection of fluorescent X-rays. A novel collection optic, a  
49 lithographically fabricated Spoked Channel Array (SCA),  
50 recently has been reported as a practical alternative for confocal  
51 micro X-ray analysis.<sup>10</sup> The basic principles and fabrication  
52 methods for SCAs have been described previously.<sup>11</sup> Employing  
53 this optic for confocal XFI enables a much smaller probing  
54 volume, allowing investigation of highly localized features as  
55 small as ~2  $\mu\text{m}$ , whereas the best-reported spatial resolution  
56 achieved from a polycapillary is ~10  $\mu\text{m}$  at 10 keV.<sup>3,12,13</sup>  
57 Additionally, the SCA optic renders the probing volume nearly  
58 independent of energy, resulting in a constant spatial resolution  
59 for different elements.<sup>10</sup> In contrast, a polycapillary derived  
60 probing volume is always energy dependent due to the energy  
61 dependency of the critical angle of total external reflection. This  
62 dependence is especially problematic for fluorescence energies  
63 below about 5 keV, for which the best reported resolution is

greater than 20  $\mu\text{m}$ .<sup>3,12,13</sup>

X-ray fluorescence imaging can be used in conjunction with X-ray absorption spectroscopy (XAS), which is a non-destructive tool for determination of the chemical form of an element. One of the strengths of the confocal detection scheme is that it enables XAS determination of the chemical form in a highly localized volume element within a thick or intact sample, which is particularly useful if heterogeneity in chemical form is expected on a scale of a few microns. Polycapillary based confocal XAS has been previously used for depth resolved chemical speciation of elements in geological and cultural heritage samples, such as Fe K XAS studies of mineral inclusions within rare natural diamonds,<sup>14</sup> Np L<sub>3</sub> XAS to determine the valence state of Np within granite,<sup>15</sup> and Cu K XAS in investigating the chemical state of coloring agents in blue and blue-green zones of Persian polychrome underglaze painted tiles.<sup>9</sup> The current paper comprises the first demonstration of SCA based confocal XAS; implementation of SCA allows superior spatial localization coupled with an energy independent probing volume. Although not demonstrated in this paper, the energy independency of probing volume will allow more straightforward correlation of chemical forms determined using more than one absorption edge.

In this paper, we demonstrate SCA based confocal XFI and XAS in investigating the distribution and speciation of elements in a medieval stained glass sample obtained from the 13<sup>th</sup> century cathedral in Paderborn, Germany. This sample, in addition to three others from the same cathedral were previously studied to determine the concentrations of elements using both laser ablation inductively coupled plasma mass spectrometry (LA-ICPMS) and synchrotron based XFI, as well as the chemical form of elements using XAS.<sup>16</sup> Elemental concentration results obtained from two techniques showed significant variation,<sup>16</sup> which was thought to be due to the presence of concentration gradients originating from corrosion or leaching layers combined with the differing surface sensitivities of the two techniques. The investigation of chemical forms of elements<sup>16</sup> employed conventional (non-confocal) XAS and highlighted the potential of the technique for revealing information on how various elements play roles in glass degradation. The XAS results<sup>16</sup> showed that although most elements in glass are found in their most stable oxidic forms, Ti and Pb show exceptions. Stained glass windows were one of the major pictorial art forms in medieval European culture with many examples still existing in their original form, for instance in churches, cathedrals and other public places. In order to optimize the cleaning, restoration and conservation procedures for these precious historical art forms and to better understand the techniques that were used in their fabrication process, it is important to explore in-depth elemental investigations as such study facilitates our understanding of the manufacturing and underlying degradation mechanisms.

The corrosion of historical glasses is a complex process determined and controlled by numerous factors such as chemical composition and characteristics of the glass, climatic conditions and atmospheric pollution.<sup>17,18</sup> The basic “corrosion mechanism” described in the literature is a two-step process in which an initial step is an ion exchange process between hydrogen-bearing species from the water film on a glass and (mainly) network-modifying ions, such as alkali and earth-alkali atoms. After the

evaporation of the water film these products form a solid weathering crust. In a subsequent step, the silica network is broken up by hydroxyl ions forming Si-OH groups and thus dissolving the glass.<sup>19</sup> To better understand the details of the mechanism of the corrosion process, depth profiling of all elements involved in this process are of interest. We demonstrate that SCA derived higher spatial resolution is useful in studying the three dimensional distribution of elements in the corrosion layer as well as their localized chemical states. Our imaging results show significant variations, within the  $\sim 100 \mu\text{m}$  outer thickness of the corrosion layer, in the concentration of iron (Fe), manganese (Mn) and calcium (Ca) which are the predominant non low-Z elements observed in the sample. In addition, spatially resolved XAS shows variation in the chemical form of Fe in the corrosion layer as a function of depth and position. This variation indicates a more complex chemistry of elements in the corrosion layer than previously described in the literature.<sup>17,19</sup> This paper demonstrates that the capability of a confocal approach in studying cultural heritage samples can be further enhanced by implementing lithographically fabricated SCA optics.

## Materials and Methods

The stained glass sample labelled as ‘Paderborn 11’ studied in this paper was recovered from an archaeological excavation at the Paderborn Cathedral, Germany carried out between 1978 and 1980.<sup>20</sup> The sample looked light green in colour under the corrosion layer. A picture of the sample is available elsewhere.<sup>16</sup>

Confocal XFI and XAS experiments were carried out at the 20ID-B (PNC/XSD) beamline of the Advanced Photon Source (APS) at the Argonne National Laboratory, with the storage ring operating in continuous top-up mode at 102 mA and 7.0 GeV. The incoming beam was tuned to an incident energy of 10 keV (estimated intensity of  $\sim 10^{12}$  photons/sec) by using a liquid-nitrogen-cooled Si (111) double crystal monochromator with a second crystal detuned by 15% to reduce harmonic contamination. A micro-beam of approximately  $5 \times 5 \mu\text{m}^2$  spot-size was produced using Rh-coated silicon Kirkpatrick-Baez (K-B)-style focusing mirrors, which also served for additional harmonic rejection. The fluorescent emission lines were monitored using an energy-dispersive single element Si-drift Vortex<sup>®</sup> detector (SII NanoTechnology USA Inc.) placed at 90° with respect to the incident X-ray beam in the horizontal plane.

To arrange the confocal geometry, a trapezoidal-shaped SCA optic, described in the next paragraph, was mounted immediately in front of the detector snout. The sample was mounted on a motorized stage at 30° to the incident beam, an angle chosen to maximize space for sample translation. An I<sub>0</sub> ionization chamber, mounted downstream of the K-B mirrors to monitor the incident monochromatized X-ray beam intensity, was used to normalize the fluorescence; this process eliminates the impact of any possible flux variations of the X-ray source on the various fluorescence spectra. A variable magnification camera focused on the sample surface was employed during set-up to view the position of beam and SCA optic relative to the sample surface, the relative positions of which were critical given the very small working distance.

The SCA optic, etched from a silicon wafer, is comprised of 96 channels each approximately  $7 \mu\text{m} \times \sim 200 \mu\text{m} \times 4 \text{ mm}$  (width  $\times$

depth  $\times$  length) in size,<sup>10</sup> and fabricated using standard lithographic techniques, including deep reactive ion etching (DRIE). The optic has a working distance of 1.0 mm, with channels separated by 9 mrad. Previous tests of this optic<sup>10</sup> demonstrated that the angular selectivity of the channels is 3.3 mrad, somewhat larger than their geometric selectivity of 1.75 mrad, and a total, effective solid angle of collection of as much as 0.14% of  $4\pi$  at 9 keV. Care was taken to block virtually all other radiation (from outside the probing volume) from reaching the detector, which is generally more challenging for SCAs than for polycapillaries. The working distance for the SCA optic used in these measurements was only a few hundred microns, although in newer versions this has been increased to about a millimeter.

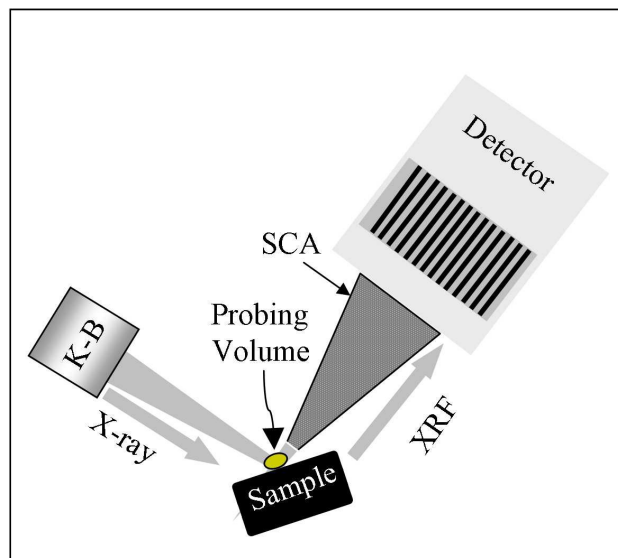


Figure 1: A schematic diagram showing Spoked Channel Array (SCA) based confocal XFI/XAS set-up. Foci of the incident (K-B) and collection (SCA) focusing optics intersect to form the probing volume.

Figure 1 shows a schematic of the confocal XFI/XAS experimental arrangement with the SCA collection optic. An initial alignment procedure allowed the intersection of focal spots of incident (K-B mirror) and collection (SCA) focusing optics in order to form the probing volume. The sample was mounted on a high precision motorized XYZ translation stage, which allowed the translation of the sample through the probing volume in three directions. The energy-independent dimension of the ellipsoidal probing volume for this configuration was  $\sim 5 \times 7 \times 4 \mu\text{m}^3$  ( $D_B \times D_A \times D_V$ ). Here  $D_B$  is one of the minor axes of the ellipsoid defined by the full-width-at-half-maximum (FWHM) of the incident beam,  $D_A$  is the major axis of the ellipsoid defined by the FWHM of the acceptance of SCA optic, and  $D_V$  is the other minor axis of the ellipsoidal probing volume, which can be calculated from the relationship  $(1/D_V)^2 = (1/D_A)^2 + (1/D_B)^2$ .<sup>14</sup> In the XYZ description presented in this paper,  $D_B$ ,  $D_A$  and  $D_V$  respectively correspond to X, Y and Z. Elemental maps were obtained by spatially rastering the sample through the probing volume along any desired plane within the sample. For the Fe K-edge confocal XAS measurement, motors were driven to the location of interest chosen from the XFI derived map with spectra recorded by scanning the energy at the XYZ location. Multiple XAS sweeps were collected at each location to verify if oxidation

state is affected by X-ray irradiation, but no such indication was observed. Data were taken with 0.3 eV steps and 3 s/p integration time through the near-edge region and to 150 eV below and 186 eV above for linear background removal and normalization to edge jump. Spectra were energy calibrated with reference to the first inflection point of a simultaneously measured Fe foil, for which the value was assumed to be 7111.3 eV. Standard spectra were reported previously.<sup>21</sup>

Confocal XFI data were analyzed using the SMAK software package.<sup>22</sup> Recorded fluorescence counts were normalized to the incident intensity and were background corrected by subtracting the average intensity of pixels outside the image from the intensity of each pixel of the image. Fe K near-edge XAS (also called Fe K-edge X-ray absorption near edge structure, or XANES) data were background subtracted and analyzed using the EXAFSPAK suite of programs.<sup>23</sup> In brief, fluorescence counts were first normalized to the incident intensity. Multiple sweeps were examined for possible spectral changes indicative of beam-induced changes, and when none were detected, the multiple sweeps were averaged. To remove background due to scatter and fluorescence from other absorption edges, a function was fitted through the below-edge region of the spectrum and was extrapolated through the remainder of the spectrum such that when subtracted, the above-edge region followed the Victoreen theoretical absorption cross-section function. Spectra were normalized by fitting a spline function through the above-edge region and then dividing by the value of the spline at 7125 eV.

The pre-edge peak region was deconvoluted similarly to the methods of Wilke et al.<sup>24</sup> using the program EDG\_FIT. For each spectrum, a 20 eV region encompassing the pre-edge peaks was fit using least-squares minimization to a background function and one or two pseudo-Voigt peak functions. Refined parameters for the peaks were the height, half-width at half height, and position. Following the method of Wilke et al.<sup>24</sup> the pseudo-Voigt mixing (amount of Gaussian versus Lorentzian) was fixed at 50% and where two or more peaks were required to fit a spectrum, the widths of the peaks were constrained to be equal. Following the calculation of peak areas, the peak centroid was calculated as the mean of the peak positions, weighted by the areas. The fit error is the sum of squares of the differences between the data and fit, normalized to the number of points in the fitted range.

Fluorescence self-absorption (also called fluorescence thickness effects) may be of concern when XAS spectra are measured on specimens which are both thick and concentrated in the target element, such that the absorption cross-section of the matrix changes significantly as a function of energy across the target absorption edge.<sup>1</sup> The phenomenon manifests itself as attenuation of high intensity spectral features concomitant with enhancement of lower intensity features. While confocal XAS samples are inherently “thick”, in our case the matrix is predominantly composed of Si, O and other non-Fe elements, such that self-absorption of Fe should be minimized. Evidence to substantiate this comes from the spectra collected at different depths, which do not appear to show no significant suppression of high intensity features or enhancement of low intensity features which would be symptomatic of this spectral artifact. Hence, no special data analysis was used to account for self-absorption in these samples.

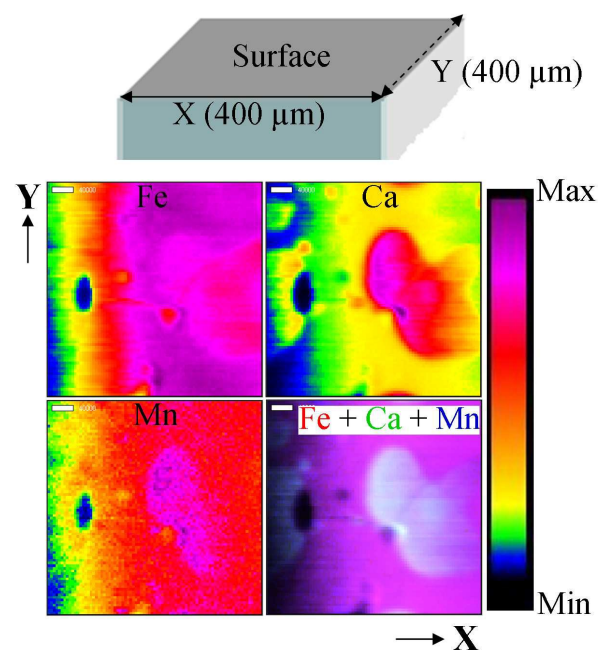


Figure 2: Elemental maps of Fe, Ca, Mn measured from a plane parallel to the surface at a depth of  $\sim 15 \mu\text{m}$ . The bar to the right gives the relative intensity scale. The bottom right map shows a superposition of Fe (red), Ca (green) and Mn (blue). The sketch at the top shows the scanning directions relative to the sample surface. Scalebar =  $40 \mu\text{m}$ .

## Results and Discussion

### Confocal XFI

Figure 2 shows elemental maps of Fe, Ca and Mn in a  $400 \times 400 \mu\text{m}^2$  scan area measured from a plane parallel to the surface, situated at a depth of  $\sim 15 \mu\text{m}$ . The map was obtained by scanning the horizontal (X) and vertical (Y) sample position motors with a  $5 \mu\text{m}$  step size and a 1 s integration time, with a total acquisition time of 2 hrs and 14 min. The bottom-right map shows the

superposition of all three elements in which Fe, Ca and Mn are respectively presented as red, green and blue. The images reveal spatial variation of the elements within the mapped area. Depth profiling of elemental distributions was achieved by recording maps of seven parallel planes, consecutively  $10 \mu\text{m}$  apart. A movie file in the Electronic Supplementary Information<sup>†</sup> shows a three dimensional reconstruction of the entire scanned volume. The specimen shows significant heterogeneity in the distribution of the measured elements within this scanned volume. In particular, in Figure 2 an oval area shows a significant enrichment in both Ca and Mn compared with surrounding areas.

Figure 3 represents elemental maps measured in a sample plane perpendicular to the plane presented in Figure 2, obtained by scanning vertical (Y) vs. normal to the sample surface (Z) axes. The direction Z corresponds to depth from the sample surface, hence this figure depicts a spatially resolved depth profile of the elemental distributions in a two dimensional view. A  $400 (Y) \times 140 (Z) \mu\text{m}^2$  area was mapped using the same acquisition settings used for Figure 2, with an acquisition time of 50 min. The scan range of  $\sim 100 \mu\text{m}$  into the sample (Z) covers a significant part of the corrosion layer, which is visible by eye as a less transparent weathering crust on the surface. In Figure 3, the interface between air and the corrosion layer at the sample surface is apparent as the sharp boundary between zero and higher intensity (dark to blue/yellow). Once again, a significant heterogeneity in the elemental distribution is observed. In particular, Fe is seen to be enriched at the surface but decreases with distance away from the surface. Conversely, Mn shows lower concentration close to the surface and a narrow band of enrichment, approximately  $10 \mu\text{m}$  wide at approximately  $60 \mu\text{m}$  below the surface. Ca also shows a high intensity band at the surface with an isolated enrichment of approximately  $150 \mu\text{m}$  wide and only about  $10 \mu\text{m}$  deep. The bands of each element persist across the entire width of the measured sample indicating a layered pattern.

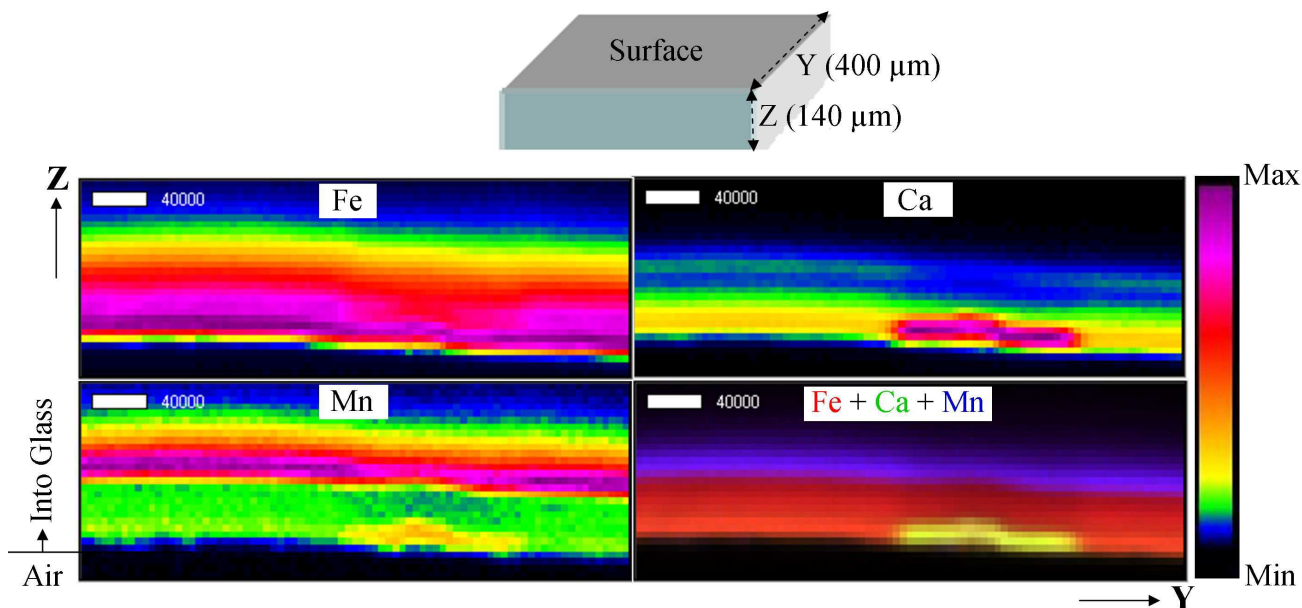


Figure 3: Elemental maps of Fe, Ca, Mn measured in a plane normal to the surface. The bar to the right gives the relative intensity scale. The bottom right map shows a superposition of Fe (red), Ca (green) and Mn (blue). The sketch at the top shows scanning directions relative to the sample surface. Zero intensity (dark) at low values of Z originates due to air. Scalebar =  $40 \mu\text{m}$ .

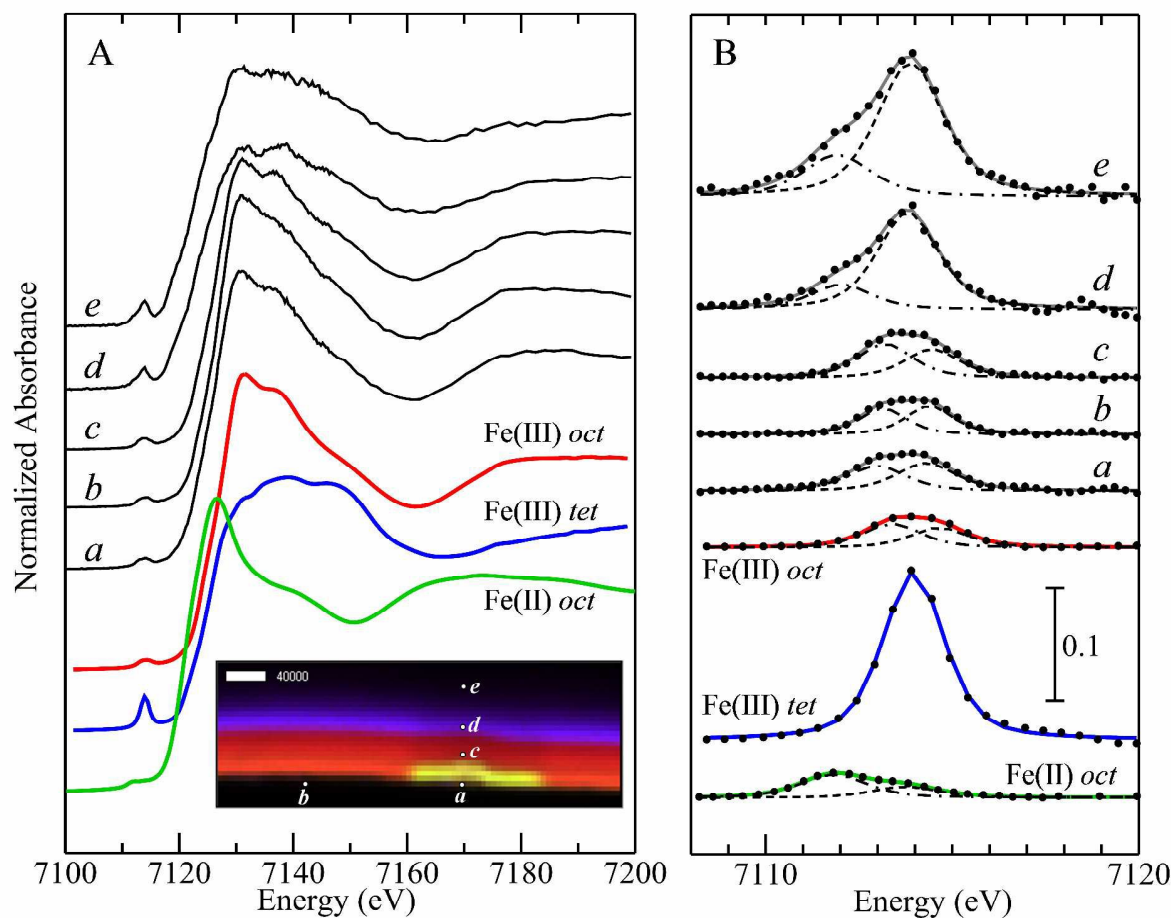


Figure 4A: Confocal Fe K-edge X-ray absorption spectra from different locations within the sample (*a-e*), as indicated in the inset (also shown in Figure 3). Spectra of Fe standards coordinated by O shown are: octahedral Fe(III) in iron substituted aluminium phosphate [Fe(III)-*oct*]; tetrahedral Fe(III) in iron substituted sodalite [Fe(III)-*tet*]; and octahedral Fe(II) in aqueous ferrous sulfate [Fe(II)-*oct*]. B: Expanded region showing the pre-edge 1s→3d peak region of the same spectra as in A, together with the results of peak-fitting (numerical values shown in Table 1). Each deconvoluted spectrum shows: data points (filled circles); fit (solid grey or coloured line); and pseudo-Voigt fitted peaks (dashed and dot-dashed lines). Both data and fit have had a background function subtracted to isolate the pre-edge features.

The medieval glass sample investigated in this study belongs to the category of wood ash glasses, which are characterized as a mixture of sand and ash from various trees; ash would have been added to the sand in order to lower the melting temperature of the glass batch.<sup>16</sup> The origin of Ca is therefore most likely from the ash.<sup>25</sup> The presence of Fe could be due to its deliberate addition in order to achieve the green colouration of the glass<sup>26</sup> or simply as an impurity of silica.<sup>27</sup> Mn similarly could be an impurity in the starting materials or added on purpose to compensate the green colour caused by Fe.<sup>28</sup> The leaching of Ca in the corrosion layer as an ion exchange process with hydrogen bearing species is a well understood phenomenon,<sup>17,19</sup> hence the observed presence of Ca in the surface region (Figure 3) is expected. Although the presence of alkaline earth ions such as Ca in the corrosion layer is well understood, a limited number of studies is available on the leaching of transition metals such as Fe or Mn into the corrosion layer.<sup>29,30</sup> Our work shows that Fe is concentrated on the surface and gradually decreases as a function of depth, whereas the concentration of Mn is low at the surface, with a buried high concentration band followed by a gradual decrease with further depth. The area of high concentration Ca with co-localized Mn evident in Figure 2 in the near surface region is another noticeable detail, whereas the high concentration Mn band does

not appear to show such co-localization. More statistics are needed to draw conclusions about such apparent patterns. A larger scale study will generate an improved understanding of the role of transition metals in the corrosion layer.

### Confocal XAS

Figure 4A shows confocally collected spatially resolved Fe K near-edge XAS measured from selected volume elements of interest in the intact sample. The acquisition time for each spectrum was 16 min. The locations were chosen according to the map shown in the inset to Figure 4, labelled *a* through *e*. Pronounced co-localization of Ca with Fe is observed in *a* whereas co-localization of Mn with Fe is observed in *d*. Locations *a* and *b* are close to the surface of the corrosion layer while *c*, *d* and *e* are successively deeper into the corrosion layer and closer to the actual glass part of the sample. Figure 4A shows clear variation in the Fe K near-edge XAS spectra, especially the position and intensity of the pre-edge peaks as well as some shifts in the rising part of the spectrum. Also presented in Figure 4A are spectra of Fe standard species. XAS can provide speciation information of elements *in situ* as spectra have characteristic features that depend on chemical environment.<sup>14,31–33</sup> The spectra of locations *a*, *b* and *c* show marked similarity to the octahedral

Table 1. Pre-edge characteristics for Fe at selected locations in the glass corrosion layer in comparison with standards as shown in Figure 4. Peak heights are normalized to an edge jump of unity. Width corresponds to the half-width at half-height. Where more than one peak is fitted for a sample, the widths of the two peaks were floated but were constrained to the same value. The fit error is the sum of squares of the differences between the data and the fitted curve, normalized to the number of points in the fitted range.

Location	Height	Position (eV)	Width (eV)	Area	Total area	Centroid (eV)	Fit error
<i>a</i>	0.0220	7112.98	0.946	0.0548	0.1164	7113.68	$1.29 \times 10^{-6}$
	0.0247	7114.30	0.946	0.0616			
<i>b</i>	0.0230	7113.15	0.751	0.0455	0.0958	7113.80	$8.91 \times 10^{-7}$
	0.0254	7114.39	0.751	0.0503			
<i>c</i>	0.0300	7113.20	0.890	0.0704	0.1299	7113.78	$8.61 \times 10^{-7}$
	0.0254	7114.46	0.890	0.0596			
<i>d</i>	0.0219	7112.02	0.973	0.0562	0.2759	7113.44	$9.10 \times 10^{-6}$
	0.0857	7113.81	0.973	0.2197			
<i>e</i>	0.0369	7111.92	1.070	0.1040	0.4368	7113.42	$7.77 \times 10^{-6}$
	0.1180	7113.88	1.070	0.3327			
Standard	Height	Position (eV)	Width (eV)	Area	Total area	Centroid (eV)	Fit error
Fe(III)- <i>oct</i>	0.0213	7113.40	0.890	0.0500	0.0915	7113.97	$3.57 \times 10^{-7}$
	0.0177	7114.65	0.890	0.0415			
Fe(III)- <i>tet</i>	0.1500	7113.97	0.980	0.3874	0.3874	7113.97	$9.37 \times 10^{-6}$
Fe(II)- <i>oct</i>	0.0204	7111.82	1.060	0.0570	0.0843	7112.44	$1.07 \times 10^{-7}$
	0.0098	7113.74	1.060	0.0273			

oxygen-coordinated Fe(III) standard (Figure 4), indicating that Fe at or near the surface of the corrosion layer is in this coordination environment. The spectra from *d* and *e* are quite distinct from those in *a* through *c*, in particular with more pronounced intensity in the region of the pre-edge peaks. The pre-edge peaks are commonly referred to  $1s \rightarrow 3d$  transitions, formally dipole-forbidden, quadrupole allowed  $\Delta l = +2$  transitions which can gain dipole-allowed intensity from admixture of 4p orbitals in non-centrosymmetric transition metal sites.<sup>24</sup>

The region of the pre-edge peaks is shown on an expanded energy scale in Figure 4B. In several studies of the pre-edge features in materials with iron-oxygen coordination,<sup>24,34,35</sup> the region of the pre-edge peaks has been found to be particularly insightful in providing information both on oxidation state and on coordination environment. Similar to these previous analyses,<sup>24,34,35</sup> Figure 4B also includes the results of deconvolution by fitting pseudo-Voigt peak functions to these features, the numerical results of which are shown in Table 1. Previous work has shown that, for single Fe species, the centroid of the pre-edge peaks is a relatively good indicator of the Fe(II) versus Fe(III) oxidation state, independent of the number or geometry of the oxygen ligands. After shifting to our calibrated energy scale, the mean centroid energies for Fe(III) and Fe(II) states are 7113.7 and 7112.3 eV respectively<sup>24</sup> other workers<sup>35</sup> show values within  $\pm 0.1$  eV. The observed centroid values for the Fe(III) and Fe(II) standards in our study, at 7114.0 and 7112.4 eV (Table 1), therefore are in good agreement with the previous observations.<sup>24,34,35</sup> The observed centroid values for all points in the glass, which range from 7113.4 to 7113.8 eV, therefore are indicative of a predominantly Fe(III) oxidation state. However, the average energy for the two deeper points, *d* and *e* (7113.4 eV), is slightly lower than the average energy of *a*, *b* and *c*

(7113.8 eV) which lie closer to the surface.

Within a given oxidation state, the integrated intensity of the pre-edge feature has been found to be indicative of the coordination geometry of the Fe-O site.<sup>24,34,35</sup> For Fe(III), the non-centrosymmetric tetrahedral sites give rise to the greatest intensity (around 0.26-0.36) while the centrosymmetric octahedral sites are lowest in intensity (around 0.06 to 0.13).<sup>24</sup> Our integrated intensity values of 0.39 and 0.09 for tetrahedral and octahedral Fe(III) standards are thus in excellent agreement. For the glass samples, spectra *a*, *b* and *c* show intensities of 0.12, 0.10 and 0.13, consistent with octahedral coordination. In contrast, the intensities of *d* and *e* are 0.28 and 0.44, which indicate a more non-centrosymmetric site and numerically show the most consistency with a tetrahedral coordination. However, whereas our tetrahedral Fe(III) standard and those of Wilke et al. show a single prominent peak in the pre-edge region, glasses *d* and *e* show intensity distributed between a prominent peak and an additional lower energy feature. This peak might be attributable to a single Fe(III) site which deviates from the ideal tetrahedral Fe(III), either by distortion or by having an intermediate 5-coordination. Alternatively, this may be explained by co-localization of different iron species, in which the dominant form is tetrahedral Fe(III) but with some admixing of another Fe type. Other authors have carried out detailed consideration of the pre-edge region in mixtures of Fe species<sup>24,34</sup> unless the spectrum of the pure end-members are known it is challenging to extract quantitative information in this situation.

Hence, our data are consistent with two environments for Fe in the glass. Near the surface of the corrosion layer (*a* through *c*) the spectra are commensurate with Fe(III) in octahedral coordination. Deeper into the corrosion layer (*d* and *e*), the spectra differ from those near the surface, still consistent with a predominantly

Fe(III) site but with a modified or mixed coordination environment. Our observation is consistent with that of Abuin et al.<sup>27</sup>, though we differ in interpretation. In their non-confocal XAS study performed on various glasses with various degrees of weathering damage, they observed a shift to lower energies of the absorption edge position as a function of decreased weathering, which they interpret as a trend from Fe(III) in weathered to Fe(II) in unweathered glass. Qualitatively we see a similar trend in a shift to lower edge energy (Figure 4) with increased depth into the sample, consistent with decreased weathering for more buried material. However, rather than to a change in oxidation state, we attribute this to a change in coordination environment of the predominantly Fe(III) site; it seems likely that this is also the case in the study of Abuin et al.<sup>27</sup>

The differences observed in the spectra demonstrate variations in the chemical form of Fe in a range of locations within a single specimen of the corrosion layer, indicating that the chemistry of metals within this layer can have significant nuances with more than a single chemical form expected. Corrosion is a complex process where depending on the nature of the glass and environment, the associated physical, chemical and electrochemical phenomena manifest differently and our results are only based on limited observations. Hence, investigation of additional specimens and elements are necessary to improve the understanding of the corrosion processes. However, our preliminary results presented herein show that establishing a relationship<sup>27</sup> between the chemical form of an element and the degradation can be especially complex due to heterogeneity of chemical form as a function of location. In non-confocal mode, determination of the chemical form of elements is limited by the contribution of XAS originating from a range of depths within the sample. Our study demonstrates that the implementation of the SCA optic for confocal XAS provides high spatial resolution as a function of depth allowing researchers to significantly extend such speciation research on medieval glasses and related specimens of historical interest.

## Conclusions

The exploitation of a SCA as a collection optic in a confocal XFI/XAS experimental configuration results in significant improvement in the spatial resolution of the experiment. Study of samples such as ancient stained glass specimens, which are often unique, fragile and require depth profiling of elements to understand the mechanisms of processes such as glass corrosion, can greatly benefit from the application of a SCA collection optic. Additionally, as the SCA derived probing volume is energy independent, the resulting energy independent spatial resolution will result in a less complicated quantification procedure compared with a polycapillary based one. In the present work, we have found that the chemical form of iron varies with locations within the sample, which is contrary to the general belief that elements in such samples are expected to be present in their most stable forms. Our results indicate that elucidating the chemical form of an element is complex as it shows spatial variation within a sample. This work is primarily focused on demonstrating the implementation of the SCA optic, and only a small area of a single specimen was investigated. The analysis of mapping and speciation on a larger scale and in additional related specimens

will provide significant information with regards to the relationship between corrosion and elements.

## Acknowledgements

This work was supported by the Canadian Foundation of Innovation through funding for BioXAS: Life Science Beamline for X-ray Absorption Spectroscopy at the Canadian Light Source Inc. This work was performed in part at the Cornell NanoScale Facility, a member of the National Nanotechnology Infrastructure Network, which is supported by the National Science Foundation (Grant ECCS-0335765). This work is based upon research conducted at the Cornell High Energy Synchrotron Source (CHESS) which is supported by the National Science Foundation and the National Institutes of Health/National Institute of General Medical Sciences under NSF awards DMR-1332208 and DMR-0936384. SC is a fellow in the Canadian Institutes of Health Research – Training grant in Health Research Using Synchrotron Techniques (CIHR-THRUST). IJP and GNG are supported by Canada Research Chair awards and research in the IJP and GNG laboratories is supported by NSERC, SHRF and CIHR. Data were collected at the PNC/XSD 20-ID-B and 20-BM-B at the Advanced Photon Source, Argonne National Laboratory. Use of the Advanced Photon Source was supported by the U. S. Department of Energy, Office of Science, Office of Basic Energy Sciences, under Contract No. DE-AC02-06CH11357.

<sup>a</sup>Department of Geological Sciences, University of Saskatchewan, 114 Science Place, Saskatoon, SK S7N 5E2, Canada. Fax: +1 306 966 8593; Tel: +1 306 966 5706; E-mail: g.george@usask.ca,

ingrid.pickering@usask.ca, sanjukta.choudhury@usask.ca

<sup>b</sup>Physics Institute, University of Bonn, Bonn 53113, Bonn, Germany. Fax: +49 228 73 7869; Tel: +49 228 73 3604; E-mail: hormes@physik.uni-bonn.de

<sup>c</sup>Cornell High Energy Synchrotron Source, Cornell University, NY 14853, Ithaca, USA. Fax: +1 607 255 9001; Tel: +1 607 255 7163; E-mail: arthurwooll@cornell.edu, da76@cornell.edu

<sup>d</sup>BioXAS, Canadian Light Source Inc., 44 Innovation Boulevard, Saskatoon, SK S7N 2V3, Canada. Fax: +1 306 657 3535; Tel: +1 306 657 3526; E-mail: Ian.Coulthard@lightsources.ca

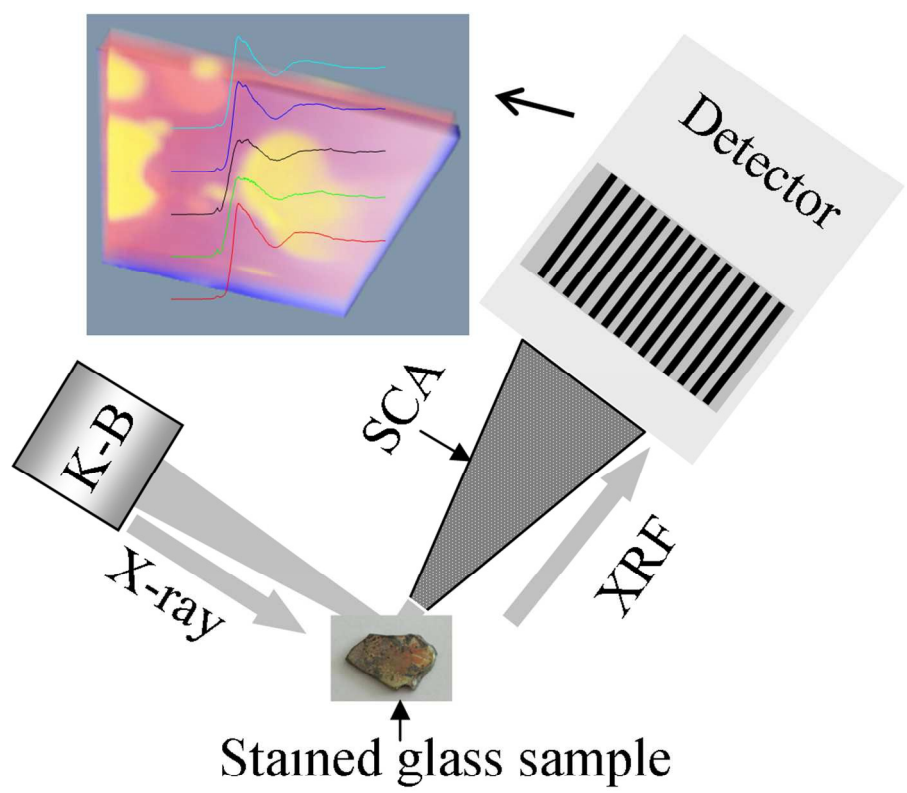
† Electronic Supplementary Information (ESI) available: A movie showing 3D elemental distribution. See DOI: 10.1039/b000000x/

## References

- M. J. Pushie, I. J. Pickering, M. Korbas, M. J. Hackett, and G. N. George, *Chem. Rev.*, 2014, **114**, 8499–8541.
- K. Janssens, K. Proost, and G. Falkenberg, *Spectrochim. Acta B*, 2004, **59**, 1637–1645.
- A. R. Woll, J. Mass, C. Bisulca, R. Huang, D. H. Bilderback, S. Gruner, and N. Gao, *Appl. Phys. A*, 2006, **83**, 235–238.
- B. Kanngießer, W. Malzer, and I. Reiche, *Nucl. Instrum. Meth. B*, 2003, **211**, 259–264.
- X. Wei, Y. Lei, T. Sun, X. Lin, Q. Xu, D. Chen, Y. Zou, Z. Jiang, Y. Huang, X. Yu, X. Ding, and H. Xu, *X-ray Spectrom.*, 2008, **37**, 595–598.
- B. Kanngießer, I. Mantouvalou, W. Malzer, T. Wolff, and O. Hahn, *J. Anal. At. Spectrom.*, 2008, **23**, 814–819.
- K. Nakano and K. Tsuji, *X-ray Spectrom.*, 2009, **38**, 446–450.
- A. Guilherme, J. Coroado, J. M. F. dos Santos, L. Lühl, T. Wolff, B. Kanngießer, and M. L. Carvalho, *Spectrochim. Acta B*, 2011, **66**, 297–307.
- I. Reiche, S. Röhrs, J. Salomon, B. Kanngiesser, Y. Höhn, W. Malzer, and F. Voigt, *Anal. Bioanal. Chem.*, 2009, **393**, 1025–1041.

10. A. R. Woll, D. Agyeman-Budu, S. Choudhury, I. Coulthard, A. C. Finnefrock, R. Gordon, E. Hallin, and J. Mass, *J. Phys.: Conf. Ser.*, 2014, **493**, 012028 (1–4).
11. A. R. Woll, D. Agyeman-Budu, D. H. Bilderback, and D. Dale, *SPIE Optics and Photonics*, 2012, **8502**, 85020K–1 – 85020K–14.
12. F. R. Sugiuro, D. Li, and C. A. MacDonald, *Med. Phys.*, 2004, **31**, 3288–3297.
13. B. Kanngießner, W. Malzer, I. Mantouvalou, D. Sokaras, and A. G. Karydas, *Appl. Phys. A*, 2012, **106**, 325–338.
14. G. Silversmit, B. Vekemans, S. Nikitenko, S. Schmitz, T. Schoonjans, F. E. Brenker, and L. Vincze, *Phys. Chem. Chem. Phys.*, 2010, **12**, 5653–5659.
15. M. A. Denecke, B. Brendebach, W. De Nolf, G. Falkenberg, K. Janssens, and R. Simon, *Spectrochim. Acta B*, 2009, **64**, 791–795.
16. J. Hormes, A. Roy, G.-L. Bovenkamp, K. Simon, C.-Y. Kim, N. Börste, and S. Gai, *Appl. Phys. A*, 2013, **111**, 91–97.
17. M. Melcher, R. Wiesinger, and M. Schreiner, *Acc. Chem. Res.*, 2010, **43**, 916–926.
18. T. Lombardo, C. Loisel, L. Gentaz, A. Chabas, M. Verita, and I. Pallot-Frossard, *Corros. Eng., Sci. Technol.*, 2010, **45**, 420–424.
19. M. Melcher and M. Schreiner, *Modern Methods for analysing Archeological and Historical Glass*, Wiley, 2013.
20. U. Lobbedey, *Die Ausgrabungen im Dom zu Paderborn 1978/80 und 1983*, Bonn : R. Habelt, 1986, vol. 1-4.
21. J. J. H. Cotelesage, M. J. Pushie, P. Grochulski, I. J. Pickering, and G. N. George, *J. Inorg. Biochem.*, 2012, **115**, 127–137.
22. S. Webb, SMAK, version 1.01, Stanford Synchrotron Radiation Laboratory, Menlo Park, CA, USA, 2012.
23. G. N. George, EXAFSPAK, University of Saskatchewan, Saskatoon, SK, Canada, 2001.
24. M. Wilke, F. Farges, P.-E. Petit, G. E. Brown Jr., and F. Martin, *Am. Mineral.*, 2001, **86**, 714–730.
25. K. H. Wedepohl and K. Simon, *Chemie der Erde*, 2010, **70**, 89–97.
26. K. H. Wedepohl, *Glas in Antike und Mittelalter – Geschichte eines Werkstoffes*, E. Schweizerbart'sche Verlagsbuchhandlung (Nägele u. Obermiller), Stuttgart, 2003.
27. M. Abuín, A. Serrano, J. Chaboy, M. A. García, and N. Carmona, *J. Anal. At. Spectrom.*, 2013, **28**, 1118–1124.
28. S. Cagno, G. Nuyts, S. Bugani, K. De Vis, O. Schalm, C. Joost, H. Lukas, M. Cotte, R. Peter, and K. Janssens, *J. Anal. At. Spectrom.*, 2011, **26**, 2442–2451.
29. O. Schalm, K. Proost, K. De Vis, S. Cagno, K. Janssens, F. Mees, P. Jacobs, and J. Caen, *Archaeometry*, 2011, **53**, 103–122.
30. J. Sterpenich and G. Libourel, *Chem. Geol.*, 2001, **174**, 181–193.
31. K. Janssens, M. Alfeld, G. Van der Snickt, W. De Nolf, F. Vanmeert, M. Radepon, L. Monico, J. Dik, M. Cotte, G. Falkenberg, C. Miliani, and B. G. Brunetti, *Annu. Rev. Anal. Chem.*, 2013, **6**, 399–425.
32. M. Wilke, K. Appel, L. Vincze, C. Schmidt, M. Borchert, and S. Pascarelli, *J. Synchrotron Radiat.*, 2010, **17**, 669–675.
33. L. Bertrand, L. Robinet, M. Thoury, K. Janssens, S. X. Cohen, and S. Schöder, *Appl. Phys. A*, 2011, **106**, 377–396.
34. W. E. Jackson, F. Farges, M. Yeager, P. A. Mabrouk, S. Rossano, G. A. Waychunas, E. I. Solomon, and G. E. Brown Jr., *Geochim. Cosmochim. Ac.*, 2005, **69**, 4315–4332.
35. G. Gabriele, G. Pratesi, C. Cipriani, and E. Paris, *Geochim. Cosmochim. Ac.*, 2002, **66**, 4347–4353.

Confocal XFI/XAS



104x104mm (300 x 300 DPI)

1  
2  
3  
4  
5  
6  
7  
8  
9  
10  
11  
12  
13  
14  
15  
16  
17  
18  
19  
20  
21  
22  
23  
24  
25  
26  
27  
28  
29  
30  
31  
32  
33  
34  
35  
36  
37  
38  
39  
40  
41  
42  
43  
44  
45  
46  
47  
48  
49  
50  
51  
52  
53  
54  
55  
56  
57  
58  
59  
60